Identification of significantly mutated regions across cancer types highlights a rich landscape of functional molecular alterations

Carlos L. Araya[1,3], **Can Cenik**[1,3], **Jason A. Reuter**[1], **Gert Kiss**[2], **Vijay S. Pande**[2], **Michael P. Snyder**[1], and **William J. Greenleaf**[1]

[1]Department of Genetics, Stanford University School of Medicine, Stanford, California, USA

[2]Department of Chemistry, Stanford University, Stanford, California, USA

[3]These authors contributed equally to this work

Abstract

Cancer sequencing studies have primarily identified cancer-driver genes by the accumulation of protein-altering mutations. An improved method would be annotation-independent, sensitive to unknown distributions of functions within proteins, and inclusive of non-coding drivers. We employed density-based clustering methods in 21 tumor types to detect variably-sized significantly mutated regions (SMRs). SMRs reveal recurrent alterations across a spectrum of coding and non-coding elements, including transcription factor binding sites and untranslated regions mutated in up to ∼15% of specific tumor types. SMRs reveal spatial clustering of mutations at molecular domains and interfaces, often with associated changes in signaling. Mutation frequencies in SMRs demonstrate that distinct protein regions are differentially mutated among tumor types, as exemplified by a linker region of PIK3CA in which biophysical simulations suggest mutations affect regulatory interactions. The functional diversity of SMRs underscores both the varied mechanisms of oncogenic misregulation and the advantage of functionally-agnostic driver identification.

Keywords

Significantly Mutated Regions (SMRs); cancer; exome sequencing; non-coding variation

Correspondence should be addressed to C.L.A. (; Email: claraya@stanford.edu), M.P.S. (; Email: mpsnyder@stanford.edu), or W.J.G. (; Email: wjg@stanford.edu)

Introduction

In cancer, driver mutations alter functional elements of diverse nature and size. For example, melanoma drivers include hyper-activating mutations at single amino acid residues (e.g. BRAF V600[1]), inactivating mutations along tumor suppressor exons (e.g. *PTEN*[1]), and regulatory mutations (e.g. *TERT* promoter[2]). Cancer genomics projects, such as the The Cancer Genome Atlas (TCGA) and the International Cancer Genome Consortium (ICGC), have substantially expanded our understanding of the landscape of somatic alterations by identifying frequently mutated protein coding genes[3–5]. However, these studies have focused little attention on systematically analyzing the positional distribution of coding mutations or characterizing non-coding alterations[6].

Algorithms to identify cancer-driver genes often examine non-synonymous to synonymous mutation rates across the gene body or recurrently mutated amino acids called mutation hotspots[5], as observed in BRAF[7], IDH1[8], and DNA polymerase ε (POLE)[9]. Yet, these analyses ignore recurrent alterations in the vast intermediate scale of functional coding elements, such as protein subunits or interfaces. Moreover, where mutation clustering within genes has been examined[10–12], analyses have employed fixed base-pair windows or identified clusters of non-synonymous mutations, assuming driver mutations exclusively impact protein sequence and ignoring the importance of exon-embedded regulatory elements[13–18].

A significant proportion of regulatory elements in the genome occurs proximal to, or even in, exons[15,19], suggesting many may be captured by whole-exome sequencing (WES). Efforts to characterize non-coding regulatory variation in cancer genomes have primarily examined either (1) pan-cancer whole-genome sequencing (WGS) data, or (2) predefined regions –such as ETS binding sites, splicing signals, promoters, and untranslated regions (UTRs)– or mutation types[20–23]. These approaches either presume the relevant targets of disruption, or disregard the established heterogeneity among cancer types at the level of driver genes and pathways[5,24,25] as well as in nucleotide-specific mutation probabilities[3,4]. Yet, systematic analyses of metazoan regulatory activity have revealed substantial tissue and developmental stage specificity[26–28], suggesting that mutations in cancer type-specific regulatory features may be significant non-coding drivers of cancer.

To address these diverse limitations, we employed density-based clustering techniques utilizing cancer-, mutation type-, and gene-specific mutation models to identify regions of recurrent mutations in 21 cancer types. This approach permitted the unbiased identification of variably-sized genomic regions recurrently altered by somatic mutations, which we term significantly mutated regions (SMRs). We identified SMRs in numerous well-established cancer-drivers as well as in novel genes and functional elements. Moreover, SMRs were associated with non-coding elements, protein structures, molecular interfaces, and transcriptional and signaling profiles, providing insight into the molecular consequences of accumulating somatic mutations in these regions. Overall, SMRs revealed a rich spectrum of coding and non-coding elements recurrently targeted by somatic alterations that complement gene- and pathway-centric analyses.

Results

Multi-scale detection of significantly mutated regions

We examined ~3 million previously identified[5] somatic, single nucleotide variants (SNVs) from 4,735 tumors of 21 cancer types, recording[29] their impact on protein-coding sequences, transcripts, and adjacent regulatory regions (Supplementary Fig. 1). Fully 79.0% (n=2,431,360) of these somatic mutations do not alter protein-coding sequences or their splicing and thus were not previously considered in the analysis of cancer-driver mutations[5] (Fig. 1a).

To discover both coding and non-coding cancer-drivers, we applied an annotation-independent, density-based clustering technique[30] to identify 198,247 variably-sized clusters of somatic mutations within exon-proximal domains of the human genome (Fig. 1b; Online Methods). We included synonymous mutations because functionally important non-coding features can be embedded within coding regions[13_18].

Mutation density scores within each identified cluster were derived as the Fisher's combined p-value of the individual binomial probabilities of observing k or more mutations for each mutation type within the region in each cancer type (Online Methods). We evaluated mutation density for each cluster using gene-specific and genome-wide models of mutation probability (Supplementary Fig. 2), which were well-correlated (Supplementary Fig. 3a), selecting the more conservative estimate for each cluster as the final density score (Online Methods). Gene-specific mutation probability models accounted for sequence composition (GC-content) as well as differences in local gene expression and replication timing, which have been shown to correlate with somatic mutation rate[4]. To avoid skewed mutation probability estimates due to selection pressure on exons, we applied a Bayesian framework to derive gene-specific mutation probabilities given intronic mutation probabilities in cancer WGS data[3,20] while controlling for differences in sensitivity in WES and WGS (Online Methods).

Although many known cancer genes do not display signals of high mutation density, increasing density scores correlated with stronger enrichments (up to 120×) for somatic SNV-driven cancer genes (n=158) as determined by the Cancer Gene Census (CGC; Supplementary Fig. 3b-c)[31,32]. Moreover, ~10% of genes associated with SMRs in the top density score quintile were not found previously in a gene-level analysis[5] or in the CGC. Thus, high density scores are enriched for known cancer genes but also nominate novel drivers.

We applied Monte Carlo simulations to select density score thresholds that control the false discovery rate (FDR) to 5% (Supplementary Fig. 4, Supplementary Table 1). We identified 872 *Significantly Mutated Regions* (SMRs; Fig. 1c) that were altered in 2% of patients in 20 cancer types for further characterization (Fig. 1d). SMRs span 735 genomic regions, which are assigned unique SMR codes (e.g. *TP53.1*). Note that some SMRs (n=120) appear in more than one cancer type.

We classified SMRs into high-, medium-, and low-confidence sets on the basis of their density scores and contribution from mutator samples (Supplementary Table 2, Online Methods). We observed correspondingly high ($63.3\times$, $P = 2.5 \times 10^{-46}$), medium ($6.2\times$, $P = 2.6 \times 10^{-10}$), and low ($5.0\times$, $P = 5.0 \times 10^{-4}$) enrichments for somatic SNV-driven cancer genes in these sets. To control for unaccounted processes that could result in clusters of mutations with no selective advantage in cancer, we leveraged single-nucleotide and tri-nucleotide density scores from intronic mutation clusters under the assumption that these are non-functional (Online Methods). This procedure identified 205 'robust' SMRs that passed a false discovery threshold (FDR 5%) in these secondary tests, or were found in multiple cancer types. Fully 95.0% of high-confidence SMRs in cancer types where these tests could be applied satisfied these stringent alternate criteria (Supplementary Fig. 5). Over 87% of SMRs were contained within mappable (100 bp) regions of the genome, and an analysis of 6,179 recently-published breakpoints[33] yielded a single SMR (in *PTEN*) within 50 bp of a resolved breakpoint, suggesting that the observed mutation density in SMRs is not attributable to mapping artifacts.

SMRs display a wide range of sizes (Fig. 1e, median = 17 bp, range 1-2,041 bp), are robust to distinct mutation background models (Fig. 1f, Online Methods), are not driven by unaccounted mutation contexts (Supplementary Fig. 6), and are enriched in protein-coding, 5′ UTR and splice-site mutations (Fig. 1g, $P < 0.01$). Importantly, SMRs are not driven by samples that contribute large numbers of mutations per region (Fig. 1h). This is in contrast to recently proposed regions of recurrent alteration[20] where as few as five were driven exclusively by distinct samples ($P = 6.0 \times 10^{-45}$, Wilcoxon rank sum test). Thus, we have identified a diverse set of variably-sized SMRs targeted by recurrent somatic alterations and sought to characterize their relevance to functional elements and cancer genes.

SMRs enrich known and implicate novel cancer genes

SMRs are predicted to have diverse impacts on 610 genes and are $8.35\times$-fold enriched in known somatic cancer genes (Lawrence et al.[5] or CGC, $P = 8.1 \times 10^{-49}$, hypergeometric test), affecting a total of 91 known drivers, including canonical oncogenes (e.g. *BRAF*, *KRAS*, *NRAS*, *PIK3CA*, and *CTNNB1*) and tumor suppressors (e.g. *PTEN*, *TP53*, and *APC*). SMR-associated genes also include 17 CGC genes previously undetected in a gene-level analysis[5], such as established oncogenes like *BCL2* and *PIM1* and the cancer-associated non-coding gene, *MALAT1*. Most coding SMRs are driven by non-synonymous mutations (Supplementary Fig. 7), demonstrating that SMRs capture positive selection primarily acting on protein alterations. In total, SMRs implicate 26 known cancer genes to an additional 31 gene-to-cancer-type associations not uncovered by a gene-level analysis[5] (Supplementary Table 3). We note, however, that most known cancer genes do not harbor regions of dense mutation recurrence within these data (see Supplementary Discussion, Supplementary Fig. 8), suggesting that SMR identification complements gene-level approaches.

We discovered SMRs in multiple novel cancer-driver genes, including the breast cancer-associated antigen and putative transcription factor ANKRD30A[34], in which ~21% of melanomas harbor mutations within one or more of three SMRs. Mutations in these SMRs

were validated in WGS data from 6 of 17 cutaneous melanomas[3,20]. Within the entire gene-body, 27 of 118 WES and 10 of 17 WGS datasets from melanoma patients harbor somatic protein-altering mutations in ANKRD30A. Overall, of the 185 high-confidence SMRs, 16 were associated with novel cancer-driver genes (Supplementary Table 4). As expected on the basis of methodological differences, these putative novel cancer-drivers are primarily (~81%) driven by non-coding alterations, as discussed in the next section.

SMRs implicate diverse non-coding regulatory features

A significant proportion (31.2%; $P < 2.2 \times 10^{-16}$, proportions test) of SMRs are not predicted to affect protein sequences, highlighting the potential to discover pathological non-coding variation in WES data. In total, 130 SMRs lay within open chromatin[28] and are enriched in promoter ($Q = 4.0 \times 10^{-9}$, 4.9×) and 5′ UTR features ($Q = 4.4 \times 10^{-10}$, 6.0×; Supplementary Table 5). Three promoter SMRs (n=26) coincide with regions deemed significantly mutated in a pan-cancer analysis of WGS data[20]. Across all cancer types, small (25 bp) non-coding SMRs were enriched in binding sequences for ETS oncogene family ($Q = 2.6 \times 10^{-6}$, 7.4×) and winged-helix repressor ($Q = 2.0 \times 10^{-4}$, 3.2×) TFs (Fig. 2a, Supplementary Table 6). We also detected cancer-specific TF motif enrichments within SMRs from diffuse large B-cell lymphoma, melanoma, and rhabdosarcoma (Fig. 2b, Supplementary Table 7).

We discovered (4 and 5 bp) SMRs within open chromatin sites of the *KIAA0907* and *YAE1D1* promoters that were altered in 10.2% and 9.3% of WES melanomas (Fig. 2c,d), respectively. Somatic mutations in these SMRs were confirmed in WGS data of melanomas (n=1 for *KIAA0907* and n=2 for *YAE1D1* of n=17, respectively)[3,20]. Yet, these regions did not reach significance in a pan-cancer analysis[20], highlighting cancer-specificity in non-coding alterations. In both SMRs, mutations alter core-recognition sequences within *in vivo* ETS factor binding sites (ENCODE), with varying effects on ETS primary sequence preferences. *KIAA0907* encodes a putative RNA-binding protein. However, intronic sequences in this gene harbor *SNORA42*, an H/ACA class snoRNA with increased expression in lung and colorectal cancer[35,36], suggesting promoter SMR alterations may enhance transcription at this locus. However, we observed no detectable changes in mutant *KIAA0907* reporter gene expression (Fig. 2e). Whereas *YAE1D1* promoter mutations reduce reporter gene expression (Fig. 2e), RNA-level overexpression of *YAE1D1* has previously been observed in lower crypt-like colorectal cancer[37], and a small cohort of melanoma samples showed increased YAE1D1 protein levels compared to untransformed melanocytes[38].

In addition to SMRs that impact promoter regions, we observed 32 SMRs in 5′ and 3′ UTRs, including putative miRNA target sites[39] Most strikingly, we discovered a 3 bp SMR in the 5′ UTR of *TBC1D12* that is mutated in ~15% of bladder cancers (Fig. 2f). Recurrent mutations were positioned near the start codon (Kozak region positions –1 and –3), suggesting a role in translational control. Mutations in this SMR were validated in whole-genome sequences of 7 cancer types, including 2 of 20 bladder cancers, 2 of 40 lung adenomas, and 3 of 172 breast cancers[3,20]. Bladder tumors with mutations in this SMR display altered RPS6KA1 (p90RSK) phosphorylation ($P = 0.0005$, *t*-test, Benjamini-

Hochberg), a signal of increased cell-cycle proliferation[40], and α-Tubulin ($P = 4.3 \times 10^{-5}$, *t*-test, Benjamini-Hochberg) levels, as determined by reverse-phase protein array (RPPA) assays[41] (Fig. 2g, Online Methods). These results establish the utility of WES data for identifying recurrently mutated non-coding regions and our SMR identification method in pinpointing potentially functional non-coding alterations in cancer.

SMRs permit high-resolution analysis of coding alterations

As expected, most exome-derived SMRs lay within protein-coding regions. The identification of SMRs across multiple cancer types permitted a systematic analysis of differential mutation frequencies with sub-genic and cancer type resolution. Although many protein domains show high burdens of somatic mutation in multiple cancers, protein domains can show remarkable cancer type-specific burdens of mutation as exemplified by VHL in kidney clear-cell carcinoma and SET in diffuse large B-cell lymphoma (Fig. 3a).

Among genes (*n*=94) with multiple SMRs, we detected 48 SMRs that are differentially mutated between cancer types (Supplementary Table 8). A striking example of this differential targeting occurs within the catalytic subunit of the phosphoinositide 3-kinase, PIK3CA (p110α), a key oncogene implicated in a range of human cancers[42,43]. We detected six SMRs in *PIK3CA* across eight cancer types (Fig. 3b), with multiple cancer types displaying SMRs in the helical (PIK3CA.5) and kinase (PIK3CA.6) domains. In contrast, we observed cancer-specific SMRs (PIK3CA.2, PIK3CA.3) affecting an α-helical region between the adaptor binding domain (ABD) and linker domains of PIK3CA. Up to 14% of uterine corpus endometrial carcinomas harbor alterations in these intron-separated SMRs although these regions are not highly recurrently altered in other cancers. For example, we observed significant ($Q = 1.2 \times 10^{-16}$, proportions test) differences in PIK3CA.2 alteration frequencies in endometrial and breast cancers (Fig. 3b) and further validated these differences ($P = 0.02$, proportions test) in whole-genome sequences[3,20]. These findings indicate that previously described differences[44] in total PIK3CA mutation frequencies between endometrial and breast cancers could in part be localized to this region.

Although the oncogenic effects of recurrent mutations in the ABD (PIK3CA.1), C2 (PIK3CA.4), helical (PIK3CA.5) and kinase (PIK3CA.6) domains of PIK3CA have been previously described, mutations in this ABD–RBD linker region are poorly understood[45–48]. Interestingly, missense mutations within this region are directionally orientated to one side of the α-helix ($P = 0.0145$, Rayleigh test), suggesting alterations to a molecular interface (Fig. 3c). Large-scale molecular dynamics simulations of PIK3CA–PIK3R1 indicate that PIK3CA.2 (K111E) and PIK3CA.3 (G118D) mutations can alter intermolecular salt bridge patterns at R79, which may result in a 1.8 kcal/mol loss of binding interactions compared to wildtype PIK3CA (Fig. 3d, Supplementary Fig. 9; Online Methods). Taken together, these results suggest a previously unrecognized mechanism of oncogenic alteration in PIK3CA.

To systematically characterize the location of alterations with respect to three-dimensional protein structures, we leveraged structural information from 428 SMR-associated and known cancer genes. We detected *n*=46 proteins with three-dimensional clustering of missense mutations (Supplementary Table 9), as exemplified by PIM1, an SMR-associated serine/threonine kinase proto-oncogene (Fig. 3e; Online Methods). This approach also identified

three-dimensional clustering between BRAF^{V600} and BRAF$^{P\text{-}loop}$ SMRs (Fig. 3f), regions where mutations have been shown to function through distinct mechanisms[49]. Moreover, we found that BRAF^{V600} mutations are more frequent in melanoma and colorectal cancers, whereas BRAF$^{P\text{-}loop}$ mutations are more common in multiple myeloma and lung adenomas ($P < 0.01$, proportions test). In total, seven of 16 proteins with multiple SMRs displayed significant SMR three-dimensional clustering (Supplementary Table 10), which is consistent with frequent spatial coherence in pathogenic alterations.

We next sought to identify SMRs that might affect the molecular interfaces of protein-protein and DNA-protein interactions, a recognized yet understudied mechanism of cancer-driver mutations[50–52]. We examined intermolecular distances between SMR residues and interacting proteins or DNA and identified 17 SMRs that likely alter molecular interfaces (Table 1; Online Methods). These include 15 molecular interfaces of protein-protein and DNA-protein interactions with established cancer associations, such as the substrate-binding cleft of SPOP[53] and DNA-binding interfaces on RUNX1 (Fig. 3g). We detected reciprocal SMRs at all electrostatic interfaces of the SMAD2–SMAD4 heterotrimer in colorectal cancer (Fig. 3h), as have been recently described[54], and reciprocal SMRs at the regulatory PIK3CA–PIK3R1 interface in endometrial cancer (Fig. 3b). Together, these results highlight the robustness of SMRs in detecting validated driver alterations in molecular interfaces (Supplementary Fig. 10). In addition, SMRs pinpoint recurrent alterations at the interface between histone H3.1 (Fig. 3i) and TRIM33, an E3 ubiquitin ligase, and at the DNA-protein interface of histone H2B (Supplementary Fig. 11). These findings underscore and extend recent associations between altered epigenetic regulation and histone alterations in tumorigenesis[55].

Molecular signatures highlight impact of SMR alterations

We sought to determine the potential functional impact of SMR alterations by their association with molecular signatures. We leveraged RNA-seq, reverse-phase protein array (RPPA), and clinical data to ask whether: (1) SMRs alterations associate with distinct molecular signatures or survival outcomes, (2) SMR alterations correlate with similar molecular profiles in distinct cancers, (3) same-gene SMR alterations associate with similar or different molecular signatures.

We found that mutations in SMRs were associated with diverse changes in RNA expression, signaling pathways, and patient survival (Fig. 4a, Supplementary Tables 11–14; Online Methods)[56]. These analyses revealed previously unappreciated connections between recurrent somatic mutations and molecular signatures, which highlight recurrent GSK3 pathway alterations in endometrial cancer and mTOR, EIF4 and EGF pathway alterations in glioblastoma (Supplementary Table 15). For example, synonymous point mutations in a bladder cancer SMR in sorting nexin 19 (*SNX19*) were associated with significant increases in protein expression levels of *RAB25* ($P = 2.5 \times 10^{-27}$, *t*-test; Fig. 4b; Supplementary Table 12), a RAS family GTPase that promotes ovarian and breast cancer progression ([57,58]. These increases are consistent with RNA expression differences of *RAB25* ($P = 0.02$; Wilcoxon rank sum test; Fig. 4c). Intriguingly, both SNX19 and RAB25 are implicated in intracellular trafficking, but the mechanism by which synonymous mutations in *SNX19* correlate with

RAB25 expression remains to be determined. In both *SNX19* and *NDUFA13*, SMRs with clusters of synonymous mutation overlap open chromatin sites[28], suggesting potential regulatory impacts.

We identified concordant changes in gene expression between SMR pairs, revealing potential functional relationships among 23 SMRs from 17 genes (Fig. 4d). These included multiple well-established mechanistic relationships, many of which were supported by RPPA measurements[41], such as between *PIK3CA* and *AKT1*. Furthermore, this analysis revealed that mutations in the same SMR in different cancers can elicit similar molecular profiles in distinct cancers. For instance, we found that SMR alterations in the oncogenic transcription factor *NFE2L2*[59] were associated with large, concordant transcriptomic changes in four distinct cancer types (bladder, endometrial, lung squamous cell carcinoma, and head and neck cancer; Fig. 4e). The four genes with the highest increases in gene expression among endometrial cancer samples with alterations in *NFE2L2.1* were the aldo-keto reductases *AKR1C1-4* (Fig. 4e), which contribute to altered androgen metabolism and have been implicated in multiple cancer types[60_62]. Across all four cancer types, transcriptomic changes associated with *NFE2L2* SMR alterations were highly enriched for oxidoreductases acting on the CH-OH group of donors, NAD or NADP as acceptors (4.9-39.0×, P 0.001, Benjamini-Hochberg, Fig. 4f). Mutations in KEAP1, a NFE2L2 binding partner, recapitulated the expression changes observed in patients with mutations in NFE2L2 SMRs (Fig. 4g; Supplementary Fig. 12; $P < 0.01$, Benjamini-Hochberg).

The identified SMRs also permitted interrogation of mutations in different regions of a given gene with respect to associated molecular signatures. For example in breast cancer, alterations in distinct SMRs within *TP53* were associated with highly similar changes in protein-levels. Yet, we observed SMR-specific differences in ASNS levels and MAPK, MEK1 phosphorylation among *TP53* SMR-altered samples (Fig. 4h, $Q < 0.01$). These results establish differences in the molecular signatures associated with same-gene SMR alterations and are consistent with pleiotropy in established oncogenes and tumor suppressors[63,64].

The structure of cancer mutations remains largely unseen

SMR analysis leverages structure in the distribution of somatic driver mutations to identify cancer-associated regions. We sought an alternative metric to assess the structure in the distribution of somatic coding mutations analyzed here by measuring the Gini coefficient of amino acid substitutions per residue in each cancer (Fig. 5a). Gini coefficients of dispersion were well-correlated with sample numbers (Spearman's $\rho = 0.74$). Subsampling demonstrates that even with sample numbers >850, a large proportion of the structure of protein-altering mutations in breast cancer remains unseen (Fig. 5b). These findings highlight the value of increasing cancer sample sizes in assessing the landscape of driver mutations.

Discussion

With few exceptions, studies of disease-associated variation have focused on identifying predefined functional units with recurrent alterations. This approach not only assumes

accurate annotations but ignores the largely uncharacterized spectrum of functional elements that may be the targets of pathologic variants. Our approach avoids these limitations and complements existing gene-level and pathway-based strategies for discovering cancer-drivers by identifying variably-sized SMRs across 20 cancer types (Supplementary Table 16). SMR-associated genes include known cancer genes, such as *PIM1* and *MIR142* that were missed by gene-level analyses, as well as multiple novel genes with potential roles in cancer development.

Cancer SMRs target a diverse spectrum of functional elements in the genome, including single amino acids, complete coding exons and protein domains, miRNAs, 5′ UTRs, splice sites, and TF binding sites among others. This functional diversity underscores both the varied mechanisms of oncogenic misregulation and the advantage of functionally-agnostic detection approaches. Notably, several of the most frequently altered SMRs lay within non-coding regions. Strikingly, 17 out of 39 promoter and 5′ UTR melanoma SMRs overlap the core recognition sequences of *in vivo* ETS-family binding sites (Odds Ratio = 15.2, $P = 1.5 \times 10^{-11}$, Fisher's exact test). In addition, ~15% of bladder cancer patients harbor 5′ UTR alterations in *TBC1D12*. Together, these results extend the support for non-coding drivers in cancer[20,23,65] and establish the potential for discovering non-coding variation in WES.

The identification of SMRs provides a sub-genic, cancer-specific analysis of somatic mutations and associated molecular signatures. Cancer type differences in SMR mutation frequencies within BRAF, EGFR, and a mechanistically uncharacterized α-helix in PIK3CA demonstrate substructure in the distribution of somatic mutations between cancers, a property that may arise from pleiotropic functions. The close geometric proximity and directional uniformity of mutations in this helix suggest that PIK3CA.2 and PIK3CA.3 mutations function through similar mechanisms. Moreover, biophysical simulations indicate that mutations in both SMRs result in an elevated basal signaling activity of catalytic PIK3CA by way of weakened interactions with the regulatory PIK3R1 protein. These findings are concordant with recent biochemical evidence[48]. Consistent with pleiotropic dependencies, alterations to SMRs within a single gene can be associated with distinct molecular signatures, as exemplified by *TP53* SMRs in breast cancers. Together, these results provide robust support for sub-genic functional targeting in distinct cancers and genes, and future efforts to examine SMR mutations in conjunction with clinical data in significantly larger patient cohorts may permit assessment of the prognostic value of SMRs.

SMR detection would benefit from further improvements of somatic mutation models. Here, we have applied cancer-specific models that take into account variation in somatic mutation rates throughout the genome. We controlled for mutational effects stemming from differences in replication timing and gene expression[4,66]. In addition, our models capture nucleotide-specific mutation probabilities[3], account for strand-specificity[67], leverage WGS mutation frequencies to limit effects from purifying selection on exons, and control mutation processes that may result in mutation clustering and tri-nucleotide mutation biases[3]. However, tumor-specific DNA repair defects[3,66,68,69] and cell-type specific chromatin context[70] also contribute to somatic mutation rates. Mutation models that account for cell-type specific expression and chromatin context at refined scales may require sequencing cohorts of matched normal tissue and increased sample sizes.

Although the sequencing of additional cancer genomes will further identification of novel cancer-driver genes[5], characterizing the biochemical and cellular consequences of individual mutations is critical. We demonstrate that identifying the spatial distribution of mutation recurrence in the genome, when combined with additional genomic, biophysical, structural, or phenotypic information, often enhances mechanistic insights. Applying recently-developed high-throughput approaches[71–73] to directly interrogate variation within SMRs may allow further understanding of the molecular mechanisms driving cancer and facilitate diagnostics and therapeutics development.

URLs

Data from Lawrence et al.[5] was obtained from the TumorPortal through: http://cancergenome.broadinstitute.org/data/per_ttype_mafs/PanCan.maf; TCGA Data Portal, https://tcga-data.nci.nih.gov/tcga; UCSC cancer browser, http://genome-cancer.ucsc.edu.

Methods

Methods and any associated references are available in the online version of the paper.

Online Methods

Scientific computing was performed within Python[74,75] and R environments. Data structure and genomic interval operations were performed with PANDAS[76] and Pybedtools[77], respectively. Statistical computing was performed with SciPy and NumPy[78], and machine learning methods were implemented with SciKit Learn[79]. Structural and sequence alignment analyses were performed with BioPython[80], PyMOL (Schrödinger) modules, and custom scripts. Reverse-Phase Protein Array (RPPA), RNA-seq, and survival analyses were performed in R and open-source packages (as described below).

Uniform Variant Annotation

3,185,590 uniformly-processed[5], whole-exome sequencing (WES) somatic variant calls from 21 cancer types were downloaded from indicated URL. We applied *snpEff*[29] to uniformly annotate *n*=3,078,482 (96.6%) single-nucleotide variant (SNV) calls from 4,735 tumors recording (GRCh37.66) mutation impact in protein-coding regions, transcribed regions (coding plus non-coding exons, introns, 5′ UTR, and 3′ UTR), and gene-associated regions (transcribed 5 kb upstream and 5 kb downstream) and standardize gene-name assignments. These procedures standardized gene-name assignments at multiple scales and removed gene assignments to "?" (*n*=64), "---" (*n*=130,728) in the original file. In addition, this procedure reduced variant calls unassigned to any genes ("Unknown", *n*=1,239,475) to *n*=899,731 intergenic calls (>5 kb from annotated exons). This procedure was also applied to annotate *n*=11,461,951 whole-genome sequencing (WGS) somatic SNV calls from 23 cancer types[3,20].

Mutation Probability Models

For each tumor type and gene, we calculated multiple distinct mutation probabilities. First, we calculated the frequency of transitions and transversions within the mappable, exonic

regions of each gene to derive 'Exonic' mutation probabilities for each gene in the hg19 human genome assembly using WES data. Specifically, these probabilities indicate the fraction of mappable (100 bp), exonic reference bases (e.g. adenines) in each gene that were somatically mutated to a specific base (e.g. cytosine) per sample, in the cohort of tumor-specific WES data.

Because expression levels and replication timing have been shown to be major co-variates of somatic mutation probability in the genome, we sought to refine our mutation probability models for each gene using this information. For each gene, and in each tumor type, we identified the set of genes most similar in the expression, replication time, and GC-content (gene-level features). We used previously compiled[4] expression and replication timing data and derived feature-specific weights defined as the rank correlation between gene features and the observed exonic mutation probabilities in each tumor type. We then converted gene features into their percentile ranks. Genes were sorted sequentially based on the gene feature weights and the neighborhood of the 500 closest genes were selected for each query gene. We then measured the sum of correlation-weighted, absolute feature distances between gene pairs within the 500 gene rank neighborhood. For each gene, we selected the 200 most similar genes with a normalized distance score 1. Lastly, we averaged the 'Exonic' mutation probability per transition/transversion to derive a set of 'Matched' mutation probabilities.

To avoid skewed mutation probabilities due to increased selection pressure on exons, we utilized a pan-cancer whole-genome sequencing (WGS)[3,20] data in conjunction with cancer-specific WES data. We employed a Bayesian framework to derive posterior mutation probabilities for each transition and transversion per gene in each of the analyzed cancer types. Specifically, we modeled the likelihood of observing a mutation as a binomial distribution. We placed a prior Beta distribution on the mutation probability for each mutation type. The prior distribution was parameterized with parameters $\alpha = \mu * \nu$ and $\beta = (1 - \mu) * \nu$, where μ is the per base mutation probability in the WES data and ν is the number of exome sequencing samples in each cancer type. This parameterization enables the variance of the prior distribution to scale inversely with the sample size. We utilized the set of genes (200) that are matched to the analyzed gene as described above. We used all observed intronic WGS mutations in this cancer-specific matched set to calculate the posterior mutation probability for the analyzed gene. In this framework, the posterior distribution is also another Beta distribution. We then assigned the expected value of the posterior probability distribution as the estimate of the mutation probability for each transition/transversion (n=12). Finally, we calibrated the posterior mutation probabilities by the cancer-specific transition/transversion rates such that the median 'Bayesian' mutation probability is equal to the mean cancer-specific 'Exonic' mutation rate.

We computed a 'Global' mutation probability per tumor type as the average probability of transitions and transversions across all genes as observed in 'Exonic' mutation probabilities in each tumor type. The distributions of WES-derived ('Exonic', 'Matched', and 'Global') as well as WGS-derived ('Bayesian') mutation probabilities varied strongly between cancer types (Supplementary Fig. 2a) and among genes within individual cancer types, highlighting the importance of such cancer- and gene-specific treatment of background mutation

probabilities[3,4]. Complementary mutation probabilities are well-correlated (Supplementary Fig. 2b). The 'Bayesian' and 'Matched' mutation probabilities are well-correlated among genes (Supplementary Fig. 2c), though 'Bayesian' mutation probabilities are better-correlated (Supplementary Fig. 2d) with the observed WGS intronic mutation densities. These 'Bayesian' (WGS-based) and 'Matched' (WES-based) mutation probabilities were used for the comparison presented in Fig. 1f.

Lastly, to account for tri-nucleotide biases[3,4] in diverse mutation processes and cancer types, we computed 'Trinucleotide' mutation probability models for each tumor type. Specifically, 'Trinucleotide' mutation probabilities were calculated as the fraction of mappable (100 bp), exonic reference bases (e.g. adenines, A) within specific tri-nucleotide contexts (e.g. CAG) that were somatically mutated to a specific base (e.g. cytosine, CAG>CCG) per sample, in the cohort of tumor-specific WES data.

Mutation Domain Definition

We extended Ensembl (75) exonic regions by 0 bp and 1,000 bp and merged regions to define n=305,145 'concise' (C) and n=191,669 'expanded' (E) genomic domains in which mutation clusters were evaluated (see below). We identified the n=279,979 'concise' and n=175,228 'expanded' domains in which over 90% of positions are fully mappable with single-end 100 bp reads (ENCODE, UCSC Genome Browser). For each set of domains, we computed the number of possible genomic ranges (start, stop), which for the 'expanded' set amounts to 1,005,774,400,023 ranges ($10^{12.0025}$). In addition, we removed 'blacklisted' regions of the human genome previously defined by the ENCODE project[81].

Mutator Sample Identification

Samples harboring aberrantly high burdens of mutations in each tumor type were detected using median absolute deviation (MAD) outlier detection on the distribution of mutations ($logn$) per sample. As a threshold for consistency, mutator (outlier) samples were selected as those exceeding two standard deviations (s.d.).

Mutation Cluster Identification

We deployed density-based spatial clustering of applications with noise (DBSCAN) to detect clusters of 2 SNVs within exonic domains (above), evaluating density-reachability within ε base-pairs in each cancer type. The reachability parameter, ε, was dynamically defined with $\varepsilon=d_p/d_s$ where d_p and d_s refer to the number of mutated positions (base-pairs) and the base-pair size of the domain d, thresholded to 10 ε 500 bp. In contrast to sliding window approaches or k-means spatial clustering, DBSCAN is not confined to evaluating predefined cluster sizes or numbers and tolerates noise in spatial density, whereby distal mutations are not assigned to clusters. Detected mutation clusters were refined where subclusters of 2 SNVs with significantly higher ($P < 0.05$, binomial test) mutation densities (mutated tumor samples per kb) existed.

Mutation Cluster Scoring

The significance of the observed mutation densities in each cluster was determined as Fisher's combined binomial probability of sampling the observed (k) or more mutations for

each mutation type within the region. For each region, we computed the above density scores with the previously described 'Exonic', 'Matched', 'Bayesian', and 'Global' somatic mutation probabilities. As the primary density score (P_{Density}), we selected the most conservative of the 'Bayesian' and 'Global' density scores, $\max(P_{\text{Bayesian}}, P_{\text{Global}})$. Finally, we computed a tri-nucleotide mutation density ($P_{\text{Trinucleotide}}$) score for each region using the 'Trinucleotide' somatic mutation probabilities.

Mutation Cluster Thresholding

We applied the procedures above to detect and evaluate mutation clusters in two sets of 'concise' (C) and 'expanded' (E) query domains (described in *Mutation Domain Definition*). 117,148/198,718 of the mutation clusters identified in E fall within the C query domains, respectively, indicating a 1.7× increase in clusters within the 1,000 bp-expanded domains.

Empirical false discovery rates (FDRs) were calculated from ten simulations performed by randomizing mutations within C domains in each tumor type, simulating a total of 30,784,820 mutations across cancer types. In each simulation, the positions of the observed mutations in each domain and tumor type, were randomized while maintaining reference base identity to retain the observed 'Global' mutation probabilities per transition and transversion (n=12). In each iteration, mutation cluster detection, refinement, and scoring procedures were repeated as above. For each simulation, we computed the density score (P_{Density}) threshold that guarantees a FDR   5%, whereby false and true discoveries are computed as the number clusters from simulated (randomized) and observed domain mutations, respectively. We excluded clusters with outlier density scores from the false discovery set if the clusters were associated with Cancer Gene Census (CGC) genes (n=522)[31,32], as these regions would not represent false discoveries. For each tumor type, the expectation value (i.e. average) of FDR   5% simulation thresholds was defined as the final tumor-specific FDR threshold. To control FDRs to   5% in the E domains, where mutations cannot be randomized owing to the decreased certainty of WES coverage, we adjusted FDRs from C domains by the 1.7× increase in E/C clusters in each tumor type. 'Expanded' (E) domain 5% FDR thresholds per tumor type are provided in Supplementary Table 1.

To assess the robustness of the FDR cutoffs, we expanded the number of simulations to 90× and confirmed a 99.2% overlap (Jaccard index) in the 5% FDR-thresholded clusters (Supplementary Fig. 4e-g).

We reiterated mutation cluster FDR estimation and filtering using an alternate, conservative density score, $P_{\text{Alternate}} = \max(P_{\text{Matched}}, P_{\text{Global}})$, resulting in 714 regions. Fully 93.2% of these regions were identified as SMRs on the basis of the primary density scores (P_{Density}).

Mutation Cluster Filtering

As a final step in calling *significantly mutated regions* (SMRs), we selected clusters with density scores (P_{Density}) at the 5% FDR threshold and that were mutated in   2% of samples in each cancer type. Lastly, clusters associated with pseudogenes, olfactory receptors, and other repetitive gene-classes, were removed. This procedure resulted in 872 significantly mutated regions (SMRs), from 735 unique genomic regions, in 20 distinct cancer types.

Mutation Cluster Annotation

SMRs were annotated on the basis of mutation impacts on coding, transcribed, and gene-associated regions (see *Uniform Variant Annotation*). For SMRs associated with multiple genes (i.e. overlapping annotations), we preferentially assigned SMRs to (1) previously known cancer-driver genes (as defined by Lawrence et al. or the CGC), or (2) the gene impacted by the most severe type of mutation. Where mutation impact was insufficient to resolve multiple gene assignments, we selected the gene impacted by the largest number of mutations within the SMR. On this basis, we assign each SMR to a single gene, recording the types of mutation impacts on the gene, and the class of region affected. Region classes include: exon (coding region and non-coding gene), intron, splice, upstream, 5′ UTR, 3′ UTR, downstream, and other (intergenic). Mutation impacts (from *snpEff*) include in order of severity: rare amino acid, splice-site acceptor, splice-site donor, start lost, stop lost, stop gained, non-synonymous coding, splice-site branch U12, non-synonymous start, non-synonymous stop, splice-site region, splice-site branch, start gained, synonymous coding, synonymous start, synonymous stop, non-coding gene ("exon"), 3′ UTR, 5′ UTR, miRNA, intron, upstream, downstream, and intergenic.

Mutation Cluster Classification

SMRs were classified into 'high-', 'medium-', and 'low-confidence' sets as follows. First, SMRs in which alterations fall below the 2% mutation frequency threshold following mutator sample (as defined above) removal were labeled as mutator-driven SMRs. Among SMRs robust to mutator removal, those with FDR-corrected density scores significant at adjusted $P < 0.05$ following Bonferroni correction ($P_{Density}$ 5.2×10^{-17}) were classified as high-confidence. Mutator-driven SMRs were classified as low-confidence. SMRs that did not meet the high-confidence or low-confidence criteria were deemed medium-confidence.

To control for unaccounted mutation processes that could result in clusters of mutations with no selective advantage in cancer, we introduced the assumption that intronic mutations are primarily composed of passenger mutations and treated intronic clusters as false discoveries. For each cancer type, the distribution of density scores from intronic mutation clusters was modeled with Gaussian Kernel-Density Estimation (KDE) to derive p-value and q-value (FDR) estimates that limit the false discovery rate to 5%. This approach is limited to the ten cancer types with sufficient intronic mutation clusters to permit KD-estimates of their distribution of mutation density scores (Supplementary Fig. 5). A threshold of n 100 intronic mutation clusters was determined on the basis of the stability of FDR thresholds as determined by subsampling intronic mutation clusters in melanoma (data not shown). We applied this approach to control false discovery rates on two metrics: First, to account for unaccounted mutation clustering, we apply this approach on our expression-, replication timing-, and sequence (GC%) composition-controlled single-nucleotide probabilities ($P_{Density}$). Second, to account for biases in tri-nucleotide mutation frequencies in each cancer type, we apply this approach on tri-nucleotide density scores ($P_{Trinucleotide}$). SMRs discovered in multiple cancer types and non-mutator-driven SMRs compliant with intron-based FDR 5% thresholds ($P_{Density}$, $P_{Trinucleotide}$ both) were classified as 'robust'.

Mutation Cluster Labeling

SMRs with higher than expected APOBEC mutation signatures[69] were labeled (Supplementary Fig. 6d, see *Mutation Trinucleotide Analysis* below). Finally, we annotated SMRs with respect to their 35 bp uniqueness and alignability with 50, 75, and 100 bp single-end reads. SMRs coordinates and corresponding annotations are provided in Supplementary Table 2.

Mutation Trinucleotide Analysis

We evaluated the frequency of trinucleotide sequence contexts as a subset of these (*TCW*) have been previously shown to differ significantly in mutation frequencies from other single-nucleotide contexts owing to APOBEC mutational processes[69]. Although APOBEC mutation signatures are identifiable in the data, our SMRs are depleted for such signatures (Supplementary Fig. 6a), suggesting the background models conservatively control for this mutation signature. Moreover, we extended these analyses to examine two important metrics:

i. unaccounted trinucleotide biases measured as the deviation in the observed trinucleotide mutation frequencies on the basis of single-nucleotide frequencies, and

ii. fold change in frequencies of trinucleotide contexts in the SMR mutations compared to the input mutations

We observed a low correlation between the unaccounted-for trinucleotide biases and the fold change in trinucleotide contexts in diverse cancer types (Supplementary Fig. 6b), further supporting the conclusion that SMRs are not driven by unaccounted-for trinucleotide mutation signatures. These analyses are restricted to cancer types (n=6) that have 250 SMR mutation sites to prevent noise from cancer types with low numbers of SMR mutations. These cancer types encompass 79% of SMRs. Across cancer types, unaccounted-for trinucleotide frequencies account for only ~7.9% of SMR sequences. For completeness, we have calculated within each SMR the fraction of mutations that are consistent with APOBEC signatures (Supplementary Fig. 6c). As shown in Supplementary Fig. 6d, only 4% of SMRs show higher than expected APOBEC mutation signatures following Holmes-Bonferroni corrected. Raw (uncorrected) *p*-values would indicate that 12% of SMRs have higher than expected APOBEC mutation signatures.

For additional methods describing (1) *Transcription Factor Motif Enrichments*, (2) *Protein Structure Mapping*, (3) *Mutation Spatial Clustering*, (4) *Mutation Dihedral Angles*, (5) *Molecular Dynamics of PIK3CA/PIK3R1 Binding*, (6) *RNA-seq Analysis*, (7) *Reverse-Phase Protein Array (RPPA) Analysis*, (8) *Functional Enrichment Analysis*, (9) *Survival Analysis*, (10) *miRNA Target Site Analysis*, and (11) *Luciferase Assays*, please see Supplementary Note.

Code Availability

The Python and R scripts to process the data and conduct the analyses described herein are available from the authors by request.

Supplementary Material

Refer to Web version on PubMed Central for supplementary material.

Acknowledgments

References

1. Hodis E, et al. A landscape of driver mutations in melanoma. Cell. 2012; 150:251–263. [PubMed: 22817889]

2. Huang FW, et al. Highly recurrent TERT promoter mutations in human melanoma. Science. 2013; 339:957–959. [PubMed: 23348506]

3. Alexandrov LB, et al. Signatures of mutational processes in human cancer. Nature. 2013; 500:415–421. [PubMed: 23945592]

4. Lawrence MS, et al. Mutational heterogeneity in cancer and the search for new cancer-associated genes. Nature. 2013; 499:214–218. [PubMed: 23770567]

5. Lawrence MS, et al. Discovery and saturation analysis of cancer genes across 21 tumour types. Nature. 2014; 505:495–501. [PubMed: 24390350]

6. Ding L, Wendl MC, McMichael JF, Raphael BJ. Expanding the computational toolbox for mining cancer genomes. Nat Rev Genet. 2014; 15:556–570. [PubMed: 25001846]

7. Davies H, et al. Mutations of the BRAF gene in human cancer. Nature. 2002; 417:949–954. [PubMed: 12068308]

8. Parsons DW, et al. An integrated genomic analysis of human glioblastoma multiforme. Science. 2008; 321:1807–1812. [PubMed: 18772396]

9. Kane DP, Shcherbakova PV. A common cancer-associated DNA polymerase ε mutation causes an exceptionally strong mutator phenotype, indicating fidelity defects distinct from loss of proofreading. Cancer Res. 2014; 74:1895–1901. [PubMed: 24525744]

10. Dees ND, et al. MuSiC: identifying mutational significance in cancer genomes. Genome Res. 2012; 22:1589–1598. [PubMed: 22759861]

11. Tamborero D, Gonzalez-Perez A, Lopez-Bigas N. OncodriveCLUST: exploiting the positional clustering of somatic mutations to identify cancer genes. Bioinformatics. 2013; 29:2238–2244. [PubMed: 23884480]

12. Porta-Pardo E, Godzik A. e-Driver: a novel method to identify protein regions driving cancer Bioinformatics. 2014; 30:3109–3114. [PubMed: 25064568]

13. Schnall-Levin M, Zhao Y, Perrimon N, Berger B. Conserved microRNA targeting in Drosophila is as widespread in coding regions as in 3′UTRs. Proc Natl Acad Sci USA. 2010; 107:15751–15756. [PubMed: 20729470]

14. Cenik C, et al. Genome analysis reveals interplay between 5′UTR introns and nuclear mRNA export for secretory and mitochondrial genes. PLoS Genet. 2011; 7:e1001366. [PubMed: 21533221]

15. Stergachis AB, et al. Exonic transcription factor binding directs codon choice and affects protein evolution. Science. 2013; 342:1367–1372. [PubMed: 24337295]

16. Wolfe AL, et al. RNA G-quadruplexes cause eIF4A-dependent oncogene translation in cancer. Nature. 2014; 513:65–70. [PubMed: 25079319]

17. Xiong HY, et al. RNA splicing. The human splicing code reveals new insights into the genetic determinants of disease Science. 2015; 347:1254806. [PubMed: 25525159]

18. Gerstberger S, Hafner M, Tuschl T. A census of human RNA-binding proteins. Nat Rev Genet. 2014; 15:829–845. [PubMed: 25365966]

19. ENCODE Project Consortium. An integrated encyclopedia of DNA elements in the human genome. Nature. 2012; 489:57–74. [PubMed: 22955616]

20. Weinhold N, Jacobsen A, Schultz N, Sander C, Lee W. Genome-wide analysis of noncoding regulatory mutations in cancer. Nat Genet. 2014; 46:1160–1165. [PubMed: 25261935]

21. Fredriksson NJ, Ny L, Nilsson JA, Larsson E. Systematic analysis of noncoding somatic mutations and gene expression alterations across 14 tumor types. Nat Genet. 2014; 46:1258–1263. [PubMed: 25383969]

22. Supek F, Miñana B, Valcárcel J, Gabaldón T, Lehner B. Synonymous mutations frequently act as driver mutations in human cancers. Cell. 2014; 156:1324–1335. [PubMed: 24630730]

23. Melton C, Reuter JA, Spacek DV, Snyder M. Recurrent somatic mutations in regulatory regions of human cancer genomes. Nat Genet. 2015; 47:710–716. [PubMed: 26053494]

24. Hofree M, Shen JP, Carter H, Gross A, Ideker T. Network-based stratification of tumor mutations. Nat Methods. 2013; 10:1108–1115. [PubMed: 24037242]

25. Leiserson MDM, et al. Pan-cancer network analysis identifies combinations of rare somatic mutations across pathways and protein complexes. Nat Genet. 2015; 47:106–114. [PubMed: 25501392]

26. Araya CL, et al. Regulatory analysis of the C. elegans genome with spatiotemporal resolution Nature. 2014; 512:400–405.

27. Stergachis AB, et al. Conservation of trans-acting circuitry during mammalian regulatory evolution. Nature. 2014; 515:365–370. [PubMed: 25409825]

28. Roadmap Epigenomics Consortium. Integrative analysis of 111 reference human epigenomes. Nature. 2015; 518:317–330. [PubMed: 25693563]

29. Cingolani P, et al. A program for annotating and predicting the effects of single nucleotide polymorphisms, SnpEff: SNPs in the genome of Drosophila melanogaster strain w1118; iso-2; iso-3. Fly. 2012; 6:80–92. [PubMed: 22728672]

30. Martin E, Kriegel HP, Jörg S, Xiaowei X. A density-based algorithm for discovering clusters in large spatial databases with noise. KDD. 1996 doi:10.1.1.71.1980.

31. Futreal AP, et al. A census of human cancer genes. Nat Rev Cancer. 2004; 4:177–183. [PubMed: 14993899]

32. Santarius T, Shipley J, Brewer D, Stratton MR, Cooper CS. A census of amplified and overexpressed human cancer genes. Nat Rev Cancer. 2010; 10:59–64. [PubMed: 20029424]

33. Malhotra A, et al. Breakpoint profiling of 64 cancer genomes reveals numerous complex rearrangements spawned by homology-independent mechanisms. Genome Res. 2013; 23:762–776. [PubMed: 23410887]

34. Jäger D, et al. Identification of a tissue-specific putative transcription factor in breast tissue by serological screening of a breast cancer library. Cancer Res. 2001; 61:2055–2061. [PubMed: 11280766]

35. Mei YP, et al. Small nucleolar RNA 42 acts as an oncogene in lung tumorigenesis. Oncogene. 2012; 31:2794–2804. [PubMed: 21986946]

36. Okugawa Y, et al. Clinical significance of SNORA42 as an oncogene and a prognostic biomarker in colorectal cancer. Gut. 2015 gutjnl–2015–309359.

37. Budinska E, et al. Gene expression patterns unveil a new level of molecular heterogeneity in colorectal cancer. J Pathol. 2013; 231:63–76. [PubMed: 23836465]

38. Uhlén M, et al. Proteomics. Tissue-based map of the human proteome Science. 2015; 347:1260419.

39. Vejnar CE, Zdobnov EM. MiRmap: comprehensive prediction of microRNA target repression strength. Nucleic Acids Res. 2012; 40:11673–11683. [PubMed: 23034802]

40. Lara R, Seckl MJ, Pardo OE. The p90 RSK family members: common functions and isoform specificity. Cancer Res. 2013; 73:5301–5308. [PubMed: 23970478]

41. Li J, et al. TCPA: a resource for cancer functional proteomics data. Nat Methods. 2013; 10:1046–1047. [PubMed: 24037243]

42. Samuels Y, et al. High frequency of mutations of the PIK3CA gene in human cancers. Science. 2004; 304:554. [PubMed: 15016963]

43. Thorpe LM, Yuzugullu H, Zhao JJ. PI3K in cancer: divergent roles of isoforms, modes of activation and therapeutic targeting. Nat Rev Cancer. 2014; 15:7–24. [PubMed: 25533673]

44. Cancer Genome Atlas Research Network. Integrated genomic characterization of endometrial carcinoma. Nature. 2013; 497:67–73. [PubMed: 23636398]

45. Miled N, et al. Mechanism of two classes of cancer mutations in the phosphoinositide 3-kinase catalytic subunit. Science. 2007; 317:239–242. [PubMed: 17626883]

46. Huang CH, et al. The structure of a human p110alpha/p85alpha complex elucidates the effects of oncogenic PI3Kalpha mutations. Science. 2007; 318:1744–1748. [PubMed: 18079394]

47. Gkeka P, et al. Investigating the Structure and Dynamics of the PIK3CA Wild-Type and H1047R Oncogenic Mutant. PLoS Comput Biol. 2014; 10:e1003895. [PubMed: 25340423]

48. Burke JE, Perisic O, Masson GR, Vadas O, Williams RL. Oncogenic mutations mimic and enhance dynamic events in the natural activation of phosphoinositide 3-kinase p110α (PIK3CA). Proc Natl Acad Sci USA. 2012; 109:15259–15264. [PubMed: 22949682]

49. Haling JR, et al. Structure of the BRAF-MEK complex reveals a kinase activity independent role for BRAF in MAPK signaling. Cancer Cell. 2014; 26:402–413. [PubMed: 25155755]

50. Kar G, Gursoy A, Keskin O. Human cancer protein-protein interaction network: a structural perspective. PLoS Comput Biol. 2009; 5:e1000601. [PubMed: 20011507]

51. Ghersi D, Singh M. Interaction-based discovery of functionally important genes in cancers. Nucleic Acids Res. 2014; 42:e18. [PubMed: 24362839]

52. Cheng F, et al. Studying tumorigenesis through network evolution and somatic mutational perturbations in the cancer interactome. Mol Biol Evol. 2014; 31:2156–2169. [PubMed: 24881052]

53. Barbieri CE, et al. Exome sequencing identifies recurrent SPOP, FOXA1 and MED12 mutations in prostate cancer. Nat Genet. 2012; 44:685–689. [PubMed: 22610119]

54. Fleming NI, et al. SMAD2, SMAD3 and SMAD4 mutations in colorectal cancer. Cancer Res. 2013; 73:725–735. [PubMed: 23139211]

55. Yuen BTK, Knoepfler PS. Histone H3.3 mutations: a variant path to cancer. Cancer Cell. 2013; 24:567–574. [PubMed: 24229707]

56. Hornbeck PV, et al. PhosphoSitePlus: a comprehensive resource for investigating the structure and function of experimentally determined post-translational modifications in man and mouse. Nucleic Acids Res. 2012; 40:D261–70. [PubMed: 22135298]

57. Cheng KW, et al. The RAB25 small GTPase determines aggressiveness of ovarian and breast cancers. Nat Med. 2004; 10:1251–1256. [PubMed: 15502842]

58. Zhang J, et al. Overexpression of Rab25 contributes to metastasis of bladder cancer through induction of epithelial-mesenchymal transition and activation of Akt/GSK-3β/Snail signaling. Carcinogenesis. 2013; 34:2401–2408. [PubMed: 23722651]

59. DeNicola GM, et al. Oncogene-induced Nrf2 transcription promotes ROS detoxification and tumorigenesis. Nature. 2011; 475:106–109. [PubMed: 21734707]

60. Ji Q, et al. Selective loss of AKR1C1 and AKR1C2 in breast cancer and their potential effect on progesterone signaling. Cancer Res. 2004; 64:7610–7617. [PubMed: 15492289]

61. Stanbrough M, et al. Increased expression of genes converting adrenal androgens to testosterone in androgen-independent prostate cancer. Cancer Res. 2006; 66:2815–2825. [PubMed: 16510604]

62. Riner TL, Šmuc T, Rupreht R, Šinkovec J, Penning TM. AKR1C1 and AKR1C3 may determine progesterone and estrogen ratios in endometrial cancer. Mol Cell Endocrinol. 2006; 248:126–135. [PubMed: 16338060]

63. Zhao L, Vogt PK. Helical domain and kinase domain mutations in p110α of phosphatidylinositol 3-kinase induce gain of function by different mechanisms. Proceedings of the National Academy of Sciences. 2008; 105:2652–2657.

64. Wu X, et al. Activation of diverse signalling pathways by oncogenic PIK3CA mutations. Nat Commun. 2014; 5:4961. [PubMed: 25247763]

65. Puente XS, et al. Non-coding recurrent mutations in chronic lymphocytic leukaemia. Nature. 2015; 526:519–524. [PubMed: 26200345]

66. Supek F, Lehner B. Differential DNA mismatch repair underlies mutation rate variation across the human genome. Nature. 2015; 521:81–84. [PubMed: 25707793]

67. Reijns MAM, et al. Lagging-strand replication shapes the mutational landscape of the genome. Nature. 2015; 518:502–506. [PubMed: 25624100]

68. Lord CJ, Ashworth A. The DNA damage response and cancer therapy. Nature. 2012; 481:287–294. [PubMed: 22258607]

69. Roberts SA, et al. An APOBEC cytidine deaminase mutagenesis pattern is widespread in human cancers. Nat Genet. 2013; 45:970–976. [PubMed: 23852170]

70. Polak P, et al. Cell-of-origin chromatin organization shapes the mutational landscape of cancer. Nature. 2015; 518:360–364. [PubMed: 25693567]

71. Araya CL, et al. A fundamental protein property, thermodynamic stability, revealed solely from large-scale measurements of protein function. Proceedings of the National Academy of Sciences. 2012; 109:16858–16863.

72. Buenrostro JD, et al. Quantitative analysis of RNA-protein interactions on a massively parallel array reveals biophysical and evolutionary landscapes. Nat Biotechnol. 2014; 32:562–568. [PubMed: 24727714]

73. Guenther UP, et al. Hidden specificity in an apparently nonspecific RNA-binding protein. Nature. 2013; 502:385–388. [PubMed: 24056935]

74. Oliphant TE. Python for Scientific Computing. Computing in Science Engineering. 2007; 9:10–20.

75. Millman KJ, Aivazis M. Python for Scientists and Engineers. Computing in Science Engineering. 2011; 13:9–12.

76. McKinney, W. Data Structures for Statistical Computing in Python. In: van der Walt, S.; Millman, J., editors. Proceedings of the 9th Python in Science Conference. 2010. p. 51-56.

77. Dale RK, Pedersen BS, Quinlan AR. Pybedtools: a flexible Python library for manipulating genomic datasets and annotations. Bioinformatics. 2011; 27:3423–3424. [PubMed: 21949271]

78. Van der Walt S, Colbert SC, Varoquaux G. The NumPy Array: A Structure for Efficient Numerical Computation. Computing in Science Engineering. 2011; 13:22–30.

79. Pedregosa F, et al. Scikit-learn: Machine Learning in Python. J Mach Learn Res. 2011; 12:2825–2830.

80. Cock PJA, et al. Biopython: freely available Python tools for computational molecular biology and bioinformatics. Bioinformatics. 2009; 25:1422–1423. [PubMed: 19304878]

81. Boyle AP, et al. Comparative analysis of regulatory information and circuits across distant species. Nature. 2014; 512:453–456. [PubMed: 25164757]
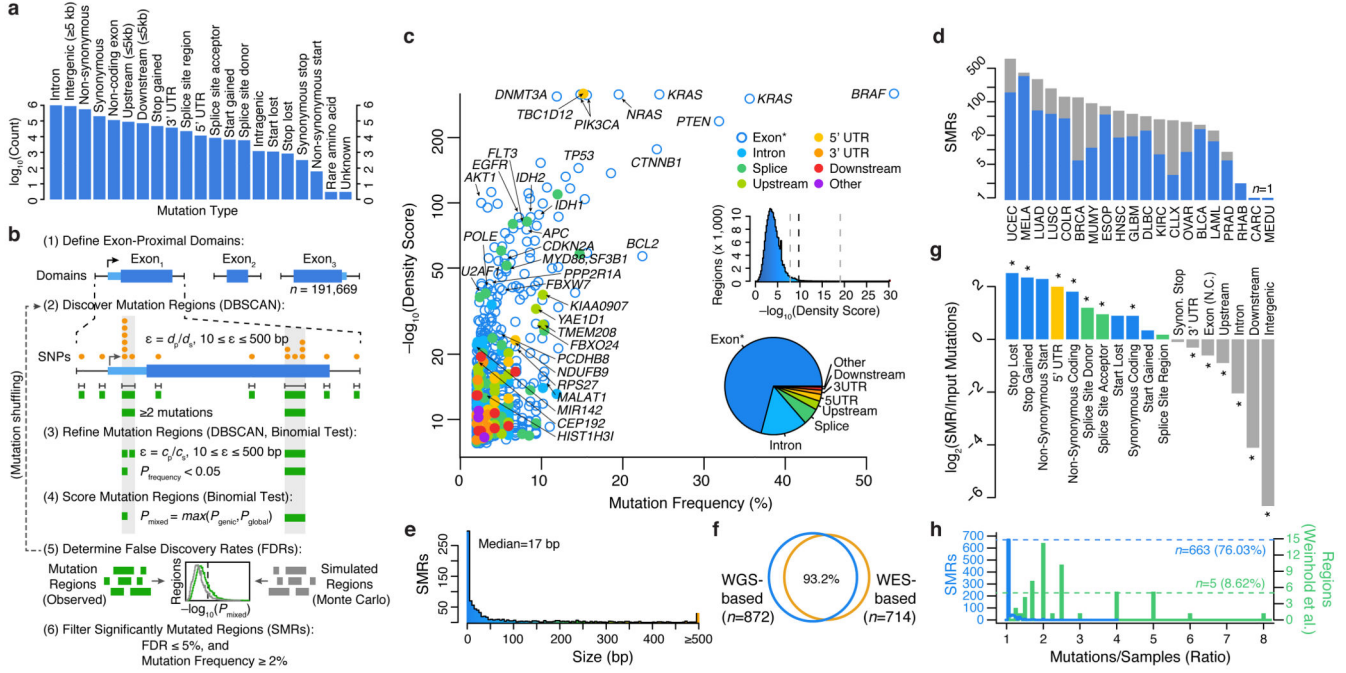
Figure 1.
Identification of significantly mutated regions (SMRs) in 20 cancer types across a broad spectrum of functional elements. (**a**) Pan-cancer distribution of mutation types in n=3,078,482 somatic single-nucleotide variant (SNV) calls. (**b**) Exons and exon-proximal domains (±1,000 bp) were scanned for clusters of somatic mutations (orange, DBSCAN). Distance parameter ε is dynamically defined as the average distance of mutated positions (d_p) in the domain size (d_s). Clusters (green) are divided if sub-clusters with higher mutation densities ($P < 0.05$, binomial test) are found in a second-pass analysis with ε defined as the average distance of mutated positions (c_p) within the cluster of size c_s (see Online Methods for density scoring and FDR calculation). (**c**) Per-cancer mutation frequency and density scores of discovered SMRs (color-coded by type and labelled by associated gene). The distribution of density scores in evaluated regions and SMR region types are shown in insets (middle) and (bottom), respectively. Dashed lines indicate the minimum, median, and maximum density score FDR (5%) thresholds. "Exon*" label refers to coding exons and non-coding genes. (**d**) Number of SMRs with FDR 5% and mutation frequency 2% per cancer type. Gray bars indicate SMRs with FDR 5% but mutation frequency <2%. (**e**) SMR size distribution. (**f**) Concordance between SMRs discovered by employing background models derived from whole-genome (WGS-based) or whole-exome (WES-based) sequencing. (**g**) Categories with significant fold change in mutation type representation between SMR-associated and input mutations are denoted (*; $P < 0.01$). (**h**) Distribution of the number of mutations per sample in SMRs (blue) and 58 (green) recurrently-altered non-coding regions[20].
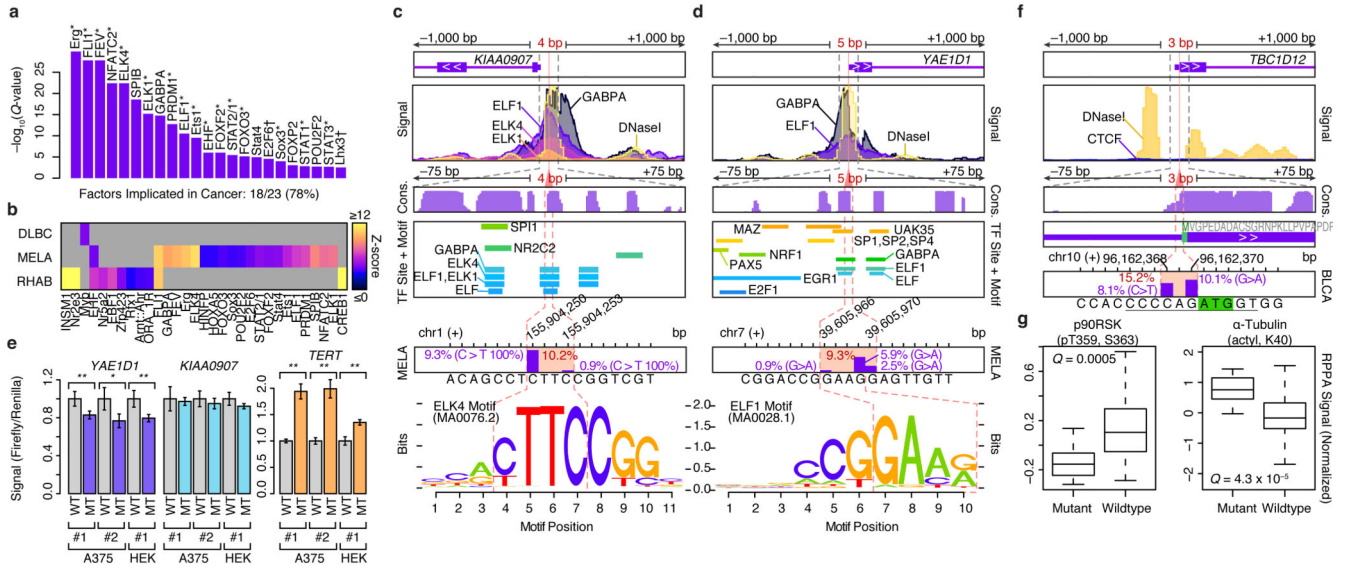
Figure 2.
Non-coding SMRs recurrently alter promoters and 5′ UTRs. (**a**) Transcription factors (TFs) with enriched ($Q < 0.01$) motifs in small SMRs (25bp) across all cancer types are shown. 18 of the 23 TFs are known cancer-associated TFs (*) or associated with cell-cycle control or developmental roles (†). (**b**) Cancer-specific motif enrichment analysis. (**c**) Gene structure, ENCODE ChIP-seq and DNaseI signals, vertebrate conservation (phastCons 100way), Factorbook TF binding sites and motif occurrences, and somatic mutation frequencies at melanoma SMRs in *KIAA0907* and (**d**) *YAE1D1* promoter regions are shown at multiple scales (±1,000, ±75, and ±7 bp). Mutation frequency within each SMR (red) and at each position (purple bars) are shown. Motifs of ETS-family binding sites that overlap the SMRs are highlighted. (**e**) Luciferase reporter signal from wildtype (WT) and mutant (MT) promoters in three experiments performed in melanoma (A375) and HEK 293T cells with independent plasmid DNA preps (#1-2). For each experiment, three replicates were performed. Luciferase/renilla signals are shown, and are normalized by the mean WT signal per experiment. Two asterisks denotes $P < 0.05$ in two-sided t-tests; one asterisk denotes $P < 0.1$. Error bars indicate s.d. (**f**) Gene-structure, ENCODE CTCF and DNaseI signals, vertebrate conservation (phastCons 100way) at the 5′ UTR *TBC1D12* bladder cancer SMR are shown at multiple scales. Start codon position is highlighted in green and Kozak sequence is underlined. (**g**) Relative protein and post-translational modification signals of wildtype (n=78) and mutant (*TBC1D12.1* SMR-altered, n=14) bladder tumors. Central band, box boundaries, and whiskers correspond to the median, the interquartile range, and the highest/lowest points within 1.5× the interquartile range, respectively.
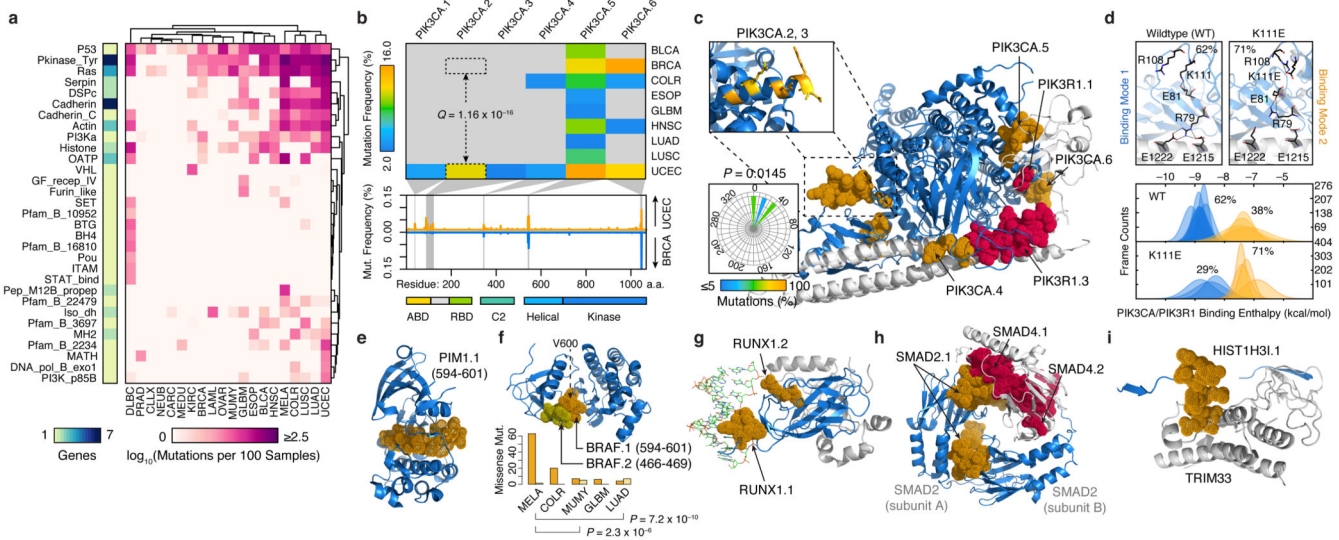
Figure 3.
Structural mapping of SMRs onto proteins and complexes reveals differentially-altered regions among cancers and molecular interfaces targeted by recurrent alterations. (**a**) Non-synonymous mutation frequency per PFAM protein domain, per cancer, per residue. Number of genes per domain is shown (left). (**b**) Mutation frequency matrix of PIK3CA SMRs across cancer types, and comparison of per residue mutation frequency of PIK3CA domains[46] in endometrial (UCEC; orange) and breast cancer (BRCA; blue) samples. Gray bars indicate SMRs within PIK3CA. (**c**) Co-crystal structure of the PIK3CA (p110α; blue) and PIK3R1 (p85α; gray) interaction (PDB: 2RDO, 2IUG, 3HIZ). Residues within endometrial cancer SMRs on PIK3CA (orange) and PIK3R1 (red) are rendered as solvent-accessible surfaces. Insets display mutated residues within the PIK3CA.2, PIK3CA.3 SMR α-helix (yellow, top) and their corresponding side-chain dihedral angles (bottom). (**d**) Molecular dynamics simulations suggest PIK3CA–PIK3R1 binding is bimodal (bottom). Mutations within the PIK3CA.2, PIK3CA.3 SMR α-helix interfere with R79 binding contacts at the PIK3R1 interface, as shown in the wildtype and K111E mutant. Molecular structures of spatially-clustered (**e**) mutations (diffuse large B-cell lymphoma) and (**f**) SMRs (multiple myeloma), (**g**) a DNA (green) interface SMR, (**h**) reciprocal protein interface SMRs, and (**i**) a histone H3.1 SMR in the TRIM33 interface. Structural alignments and molecular visualizations prepared with PyMOL (Schrödinger). The relative proportions of BRAF.1 and BRAF.2 missense mutations per cancer type are shown in (**f**). PDB codes for (**e-i**) are 3CXW, 1UWH, 1H9D, 1U7V, and 3U5N, respectively.
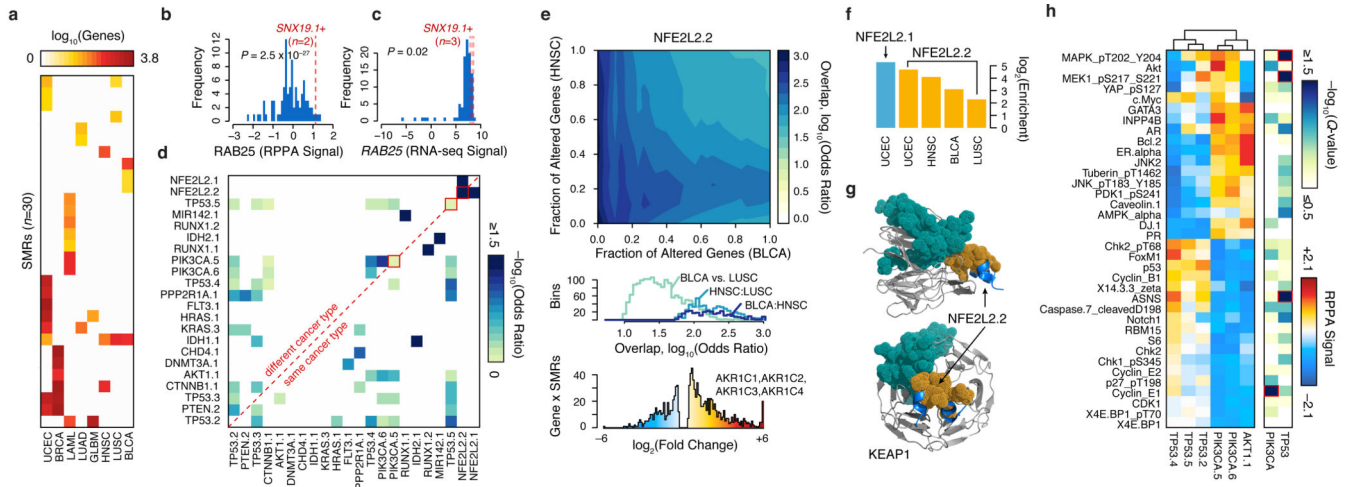
Figure 4.

SMRs are associated with distinct molecular signatures. (**a**) Matched RNA-seq data for nine cancers revealed that mutations in 30 distinct SMRs associated with 10 differentially expressed genes (FDR < 5%). (**b**) Normalized reverse phase protein array (RPPA) and (**c**) RNA-seq signals for *RAB25* are plotted. Red lines indicate signals for samples with mutated *SNX19* SMR. (**d**) Similarity between differentially expressed gene sets associated with mutations in each SMR pair. (**e**) Overlap between differentially expressed genes associated with altered NFE2L2.2 in bladder cancer (BLCA) and head and neck carcinoma (HNSC) is shown (top). Differentially expressed genes are sorted by *p*-value and similarity is quantified by Fisher's exact test odds ratio. The distribution of odds ratios of similarity is summarized for three comparisons (middle). Samples with NFE2L2.2 mutations exhibit highly increased expression of aldo-keto reductase enzymes (bottom). (**f**) The relative enrichment for oxidoreductase activity (GO:0016616) for specific cancer types (Supplementary Table 13). (**g**) Structure of SMR NFE2L2.2 (orange) in the KEAP1-binding domain (PDB: 3WN7). A sector of recurrent alterations on KEAP1 (teal) did not pass our 2% frequency cutoff. (**h**) Breast cancer patients were grouped by mutations in six SMRs in PIK3CA, AKT1, and TP53. Normalized RPPA-based expression was obtained from The Cancer Proteome Atlas (TCPA)[41]. The median RPPA signal for 36 markers and *q*-value (Kruskal-Wallis test) of differential expression between SMRs of TP53 or of PIK3CA are plotted (red highlights markers with significant intragenic differences, $Q < 0.05$).
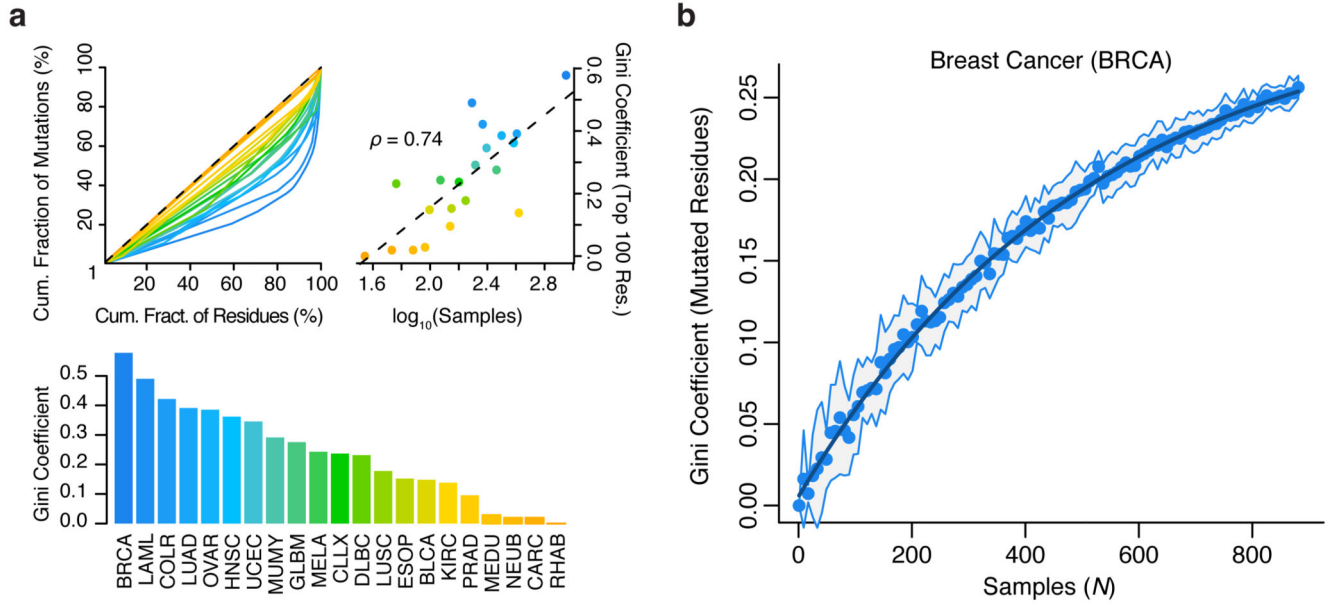
Figure 5.
Structure in the distribution of cancer mutations remains largely uncharacterized. Gini coefficients of dispersion were calculated as the fraction of non-synonymous mutations contained per residue, across ~19,000 proteins. (**a**) Lorenz curves (top-left), Gini-coefficients (top-right), and their correlation with tumor sample numbers (bottom) are shown. (**b**) Gini coefficients of non-synonymous mutation frequency in breast cancer as a function of (bootstrapped) sample size. Line of exponential fit is shown in dark blue. For comparisons between cancer types (**a**), the Gini coefficients were computed exclusively on the 100 most mutated residues per cancer.

Table 1

Recurrently altered protein interfaces uncovered by SMRs

Protein (i)	Partner (j)	PDB	Chain (i)	Chain (j)	Region	Avg. Distance (Å)	Distance Ratio	Q-value	Status
VHL	TCEB1	3ZUN	I	H	chr3:10191469:10191513	7.259	0.395	7.62×10^{-10}	Known
VHL	TCEB2	1LQB	C	A	chr3:10191469:10191513	9.867	0.367	7.62×10^{-10}	Known
SPOP	H2AFY	3HQH	A	M	chr17:47696421:47696467	7.962	0.462	3.72×10^{-8}	Known
SMAD2	SMAD4	1U7V	A	C	chr18:45374881:45374945	9.231	0.460	5.61×10^{-8}	Known
HIST1H2BK	DNA	2CV5	D	J	chr6:27114446:27114519	9.730	0.520	3.27×10^{-7}	Novel
TP53	TP53BP1	1KZY	B	D	chr17:7578369:7578556	13.253	0.556	5.13×10^{-7}	Known
SMAD4	SMAD2	1U7V	B	C	chr18:48604665:48604797	11.878	0.694	5.13×10^{-7}	Known
DNMT3A	DNMT3L	2QRV	E	F	chr2:25463271:25463308	10.112	0.380	5.13×10^{-7}	Known
SMAD4	SMAD3	1U7F	B	C	chr18:48604665:48604797	11.883	0.700	1.94×10^{-6}	Known
PIK3CA	PIK3R1	3HHM	A	B	chr3:178936070:178936099	9.028	0.335	2.56×10^{-6}	Known
RUNX1	DNA	1H9D	C	H	chr21:36231782:36231792	8.957	0.351	0.001	Known
HIST1H3I	TRIM33	3U5N	D	A	chr6:27839651:27840062	11.480	0.610	0.001	Novel
HIST1H2BK	HIST1H4*	2CV5	D	F	chr6:27114446:27114519	13.680	0.664	0.002	Novel
PPP2R1A	PPP2R5C	2NPP	D	E	chr19:52716323:52716329	7.313	0.247	0.007	Known
HRAS	RASA1	1WQ1	R	G	chr11:534283:534291	5.302	0.350	0.007	Known
PIK3R1	PIK3CA	3HIZ	B	A	chr5:67589138:67589149	6.713	0.567	0.008	Known
NFE2L2	KEAP1	2FLU	P	X	chr2:178098799:178098815	6.157	0.566	0.009	Known
EGFR	EGF	3NJP	B	A	chr7:55233035:55233043	8.763	0.386	0.019	Known
FGFR2	FGF8	2FDB	R	M	chr10:123279674:123279677	10.288	0.413	0.036	Known
FBXW7	SKP1	2OVR	B	C	chr4:153249384:153249385	9.352	0.346	0.036	Known
FGFR2	FGF2	1EV2	H	A	chr10:123279674:123279677	11.685	0.406	0.037	Known

*
Indicates multiple components partner proteins identified. "Status" indicates whether the SMR-harboring protein (i) is a known or novel cancer-driver gene.